Int. J. Solids Structures Vol. 27, No. 10, pp. 1327–1346, 1991
Printed in Great Britain.

0020–7683/91 $3.00+.00

THE EFFECTS ON PENETRATOR DECELERATION OF MATERIAL FEATURES EXHIBITED IN SOILS

H. L. SCHREYER and C.-P. CHIU
Department of Mechanical Engineering, University of New Mexico, Albuquerque, NM 87131, U.S.A.

(*Received* 28 *December* 1989; *in revised form* 19 *June* 1990)

Abstract—The nonlinear finite element method is used to solve the axisymmetric one-dimensional penetration problem for conical and ogival nose shapes. An elastic–plastic theory is used in which the yield surface consists of a Prager–Drucker surface and a planar cap. Existing analytical solutions are used to verify the numerical procedure. The constitutive features investigated include strain hardening, strain softening, rate dependence and various forms for the hydrostat. Interface conditions are assumed to be Coulomb friction, fluid layer and no slip. Assumptions are evaluated by comparing predictions of the resultant retarding force on the penetrator to experimental data. Results indicate that strain hardening of the Prager–Drucker yield surface is of some significance but that rate effects associated with this surface are insignificant. On the other hand, both strain hardening and rate effects for the cap part of the model are very important features. The use of a strain softening yield surface results in the prediction of a hydrostatic layer. This effect is observed in some experimental tests. Separation of the soil from the penetrator is predicted for the ogival penetrator for sufficiently high velocities of penetration. Overall, the procedure provides a method for evaluating the relative importance of constitutive features to the penetration process and shows how penetrator acceleration data can be used to assist in determining material parameters.

INTRODUCTION

The correlation of material parameters with accelerometer data from a rigid penetrator has the potential for several important engineering applications (Backman and Goldsmith, 1978). Examples include the determination of ice thickness, the compositions of earth media in remote areas and the design of foundations and anchors. There have been claims of excellent correlation between accelerations and specific material parameters for soils, but on closer inspection, many of the models for which the material parameters are defined are suitable only for static problems and small strains. In reality, the deformation is large in the vicinity of a penetrator with significant impact velocity and the strain rates are high. In soils, the large deformations are often localized within a small but finite zone adjacent to the penetrator. In order to predict such a zone with the use of a continuum approach, softening and, perhaps, a nonlocal feature must be included in the model. Other important features such as strain hardening, rate effects, shear enhanced compaction and alternative interface conditions are normally not included. Therefore, claims of a direct relation between material parameters and acceleration data must be suspect if these features have not been included.

Previous investigations of dynamic penetration can be categorized as follows: (a) empirical equations to obtain final depth of penetration based on full-scale test results, (b) detailed numerical solutions utilizing one- and two-dimensional codes, and (c) analytical solutions based on cylindrical and spherical expansions to obtain a one-dimensional equation for describing the response of the penetrated media.

Young (1969, 1972, 1976) has developed empirical equations and techniques based on over 500 full-scale earth penetration tests. The equations are applicable for both conical and more complex penetrators, and for homogeneous and layered earth media. His approach can provide a deceleration profile and predict the depth of penetration to within $\pm 20\%$. However, this procedure provides very little information for evaluating constitutive relations of the target media.

For normal penetration, where it is assumed that the penetrator strikes the surface of the earth perpendicularly and that the penetrator does not change direction, the problem is two-dimensional and amenable to numerical analysis provided care is taken to handle the potential problem of the singularity that appears with a nonzero radial displacement

along the penetrator axis. Numerous studies have been performed (Byers and Chabai, 1977; Byers *et al.*, 1975, 1978; Thigpen, 1974) in which good correlations with experimental data have been reported. However, an examination of the constitutive equations used for these studies show that elastic–plastic models with no rate dependence have been used. For the most part, only the failure part of these models has been constructed to represent static experimental data; no attempt has been made to describe dilatation, shear enhanced compaction, increase in ductility with mean pressure, softening and localization. Since the models do not accurately reflect soil behavior, there must be a reason for the good correlation. One possible explanation is that the penetrator resistance is an integrated effect in which the result of each soil response feature is smeared and the effects of several features are countervailing. One purpose of this investigation is to determine whether several constitutive features provide compensating effects and, if so, to show how individual characteristics can be separated.

Since the constitutive equation is nonlinear and large deformations occur, it is not reasonable to expect analytical solutions. However, a similarity approach involving cylindrical and spherical cavity expansions converts the partial differential equations to a single nonlinear ordinary differential equation from which numerical solutions can be obtained. Analytical solutions are available with additional linearizing assumptions (Norwood, 1974; Longcope and Grady, 1978; Forrestal *et al.*, 1981a,b; Longcope and Forrestal, 1981; Forrestal and Longcope, 1982; Norwood and Sears, 1982; Longcope and Forrestal, 1983). Again, elastic–plastic models are used; however, the great value of these contributions is that there are no hidden approximations associated with the spatial discretization associated with numerical procedures and the solutions provide limiting cases for verifying computational procedures. Furthermore, many of these analyses have been substantiated with experimental data obtained under carefully controlled conditions (Forrestal, 1983, 1985; Forrestal and Grady, 1982; Forrestal *et al.*, 1984a,b, 1986). The cylindrical cavity expansion approach involves the assumption that the motion of the target material is strictly radial. This study, a synopsis of the work by Chiu (1988), utilizes the same assumption which renders the problem one-dimensional in space.

A large amount of penetrator data is available for soils so the opportunity to evaluate procedures for using these data to determine material properties exists. To make this correlation, solutions to the governing equations are required. Here, the nonlinear finite element method is used to solve the axisymmetric one-dimensional penetration problem for conical and ogival nose shapes. Existing analytical solutions are used to verify the numerical procedure. Constitutive features that are investigated include strain hardening, strain softening, rate dependence and various forms for the hydrostat. Interface conditions that are investigated include variable Coulomb friction and a fluid layer with various pressures. The effects are described in terms of stress profiles in both space and time and of the resultant retarding penetrator force. Assumptions are evaluated by comparing predictions of the resultant retarding force on the penetrator to experimental data. Results indicate that strain hardening of the Prager–Drucker yield surface is of some significance but that rate effects associated with this surface are insignificant. On the other hand, both strain hardening and rate effects for the cap part of the model are very important features. Conclusions concerning interface assumptions are less clear although the use of a strain softening yield surface results in the prediction of a hydrostatic layer which is observable in some experimental tests. Separation of the soil from the penetrator is predicted for the ogival penetrator for sufficiently high velocities of penetration.

GOVERNING EQUATIONS

Penetrator nose geometry

Consider the geometrical configurations shown in Fig. 1 for conical and ogival penetrators impacting perpendicularly to the surface of a semi-infinite soil medium. A Lagrangian cylindrical coordinate system is constructed so that the penetrator makes initial impact with the soil at the origin of the R–Z plane where Z is positive in the direction of penetrator motion. Let the length of the nose be L and the afterbody radius be R_f. The geometry of

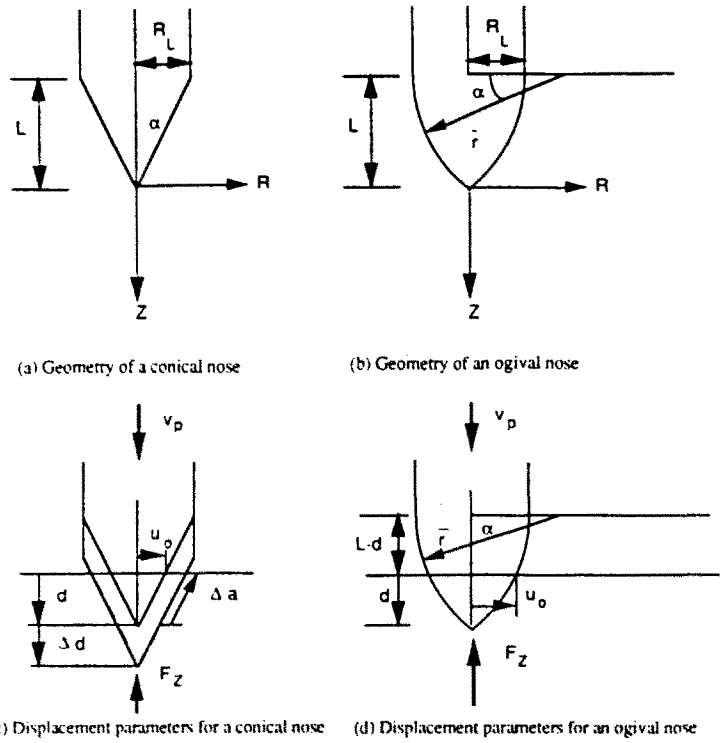

(a) Geometry of a conical nose (b) Geometry of an ogival nose

(c) Displacement parameters for a conical nose (d) Displacement parameters for an ogival nose

Fig. 1. Parameters associated with penetrators in earth media. (a) Geometry of a conical nose, (b) geometry of an ogival nose, (c) displacement parameters for a conical nose, and (d) displacement parameters for an ogival nose.

the conical nose is defined by the angle α with $\tan \alpha = R_l/L$ and the geometry of the ogival nose by the caliber radius head, $C_{RH} = \bar{r}/2R_l$, in which $\bar{r}$ is the radius of curvature used to shape the nose. If the direction of penetration does not change (normal penetration) the problem is two-dimensional in the R–Z plane. If, in addition, motion is assumed to be radial and each layer perpendicular to the Z-coordinate acts independently of adjacent layers (no shear stress in the R–Z plane), then the result is a one-dimensional problem. If the resistive force along the cylindrical afterbody of the penetrator behind the nose is negligible, then the resultant retardation force for a given penetrator can be determined by analyzing the penetrator nose while it penetrates a distance equal to the length of the nose. The penetration velocity, v_p, is assumed to be constant for the analysis. Since the experimental data considered here are in terms of acceleration, and not depth of penetration, no attempt is made to follow a penetrator until it comes to rest. Instead, the one-dimensional study is limited to the time it takes the penetrator nose to become completely embedded. However, because of the one-dimensional assumptions, the analysis for penetration is identical for all starting locations of the nose tip including that of the free surface defined by $Z = 0$.

If $\boldsymbol{\sigma}$ is the Cauchy stress tensor, the traction is given by $\mathbf{t} = \boldsymbol{\sigma} \cdot \mathbf{n}$ for a surface with outer normal $\mathbf{n}$. The traction on the penetrator is equal and opposite to that of the surface of the soil, so for the cylindrical system (R, Z, θ) of Fig. 1, the axial component of the traction acting on the penetrator is

$$t_Z = -\sigma_{ZZ} \sin \alpha; \tag{1}$$

with the assumption that $\sigma_{ZR} = 0$. For an increment in time of Δt the increment in axial displacement is $\Delta d = v_p \Delta t$ and the increment in retarding force is

$$\Delta F_z = t_z \Delta A \quad \text{with} \quad \Delta A = 2\pi u_0 \Delta a \quad \text{and} \quad \Delta a = \frac{\Delta d}{\cos \alpha}. \tag{2}$$

in which ΔA is the increment in area of the projectile exposed to the soil. The horizontal displacement of a material point at the origin is u_0, and Δa is the additional length of nose that has come in contact with the soil. When (1) and (2) are combined, the result is

$$\Delta F_z = -2\pi \Delta t \sigma_{zz} v_p u_0 \tan \alpha. \tag{3}$$

If $t = 0$ corresponds to the time when penetration starts, the following explicit expressions follow for the conical penetrator:

$$u_0 = t v_p \tan \alpha \quad \Delta F_z = -2\pi t \Delta t v_p^2 \tan^2 \alpha. \tag{4}$$

For the case of an ogive, α is not a constant but varies with d according to

$$\tan \alpha = \frac{L - d}{\sqrt{\bar{r}^2 - (L-d)^2}}. \tag{5}$$

Since $\bar{r}^2 - L^2 = (\bar{r} - R_t)^2$, the radial displacement at the origin becomes

$$u_0 = R_t - \bar{r} + \sqrt{\bar{r}^2 - (L-d)^2}. \tag{6}$$

To obtain the increment in force, (5) and (6) are substituted into (3).

Interface assumptions

With the assumption of purely radial motion and continued soil contact with the penetrator nose, the boundary condition for the penetrated medium is completely specified. With the assumption that Coulomb's law applies, there is an inherent contradiction unless the coefficient of friction, ζ, is assumed to vary with the stress components such that

$$\zeta \equiv \frac{|t_t|}{|t_n|} = \frac{-\sigma_{RR} + \sigma_{zz}}{\sigma_{RR} + \sigma_{zz} \tan^2 \alpha} \tan \alpha; \tag{7}$$

where t_t and t_n are the components of the traction tangential and normal to the penetrator, respectively. The stress components are evaluated at $R = 0$ and result from the solution to the governing equations. If the resultant state of stress is hydrostatic, then ζ must be zero. If ζ is specified, then the one-dimensional restriction must be relaxed and the problem becomes two- or three-dimensional.

Initially, Longcope and Forrestal (1983) assumed zero friction with the implication from (7) that $\sigma_{zz} = \sigma_{RR}$. In addition, they set $\sigma_{\theta\theta} = \sigma_{zz}$, which defines a hydrostatic state of stress adjacent to the penetrator. There is some post-test evidence (Forrestal and Grady, 1982) of surface melting of the nose and some wear on the aft body, which supports the concept of a hydrostatic layer. Longcope and Forrestal (1983) also added a frictional term associated with a nonzero coefficient of friction by arguing that for small cone angles ($\tan \alpha < 0.3$) and small values of the coefficient of friction ($\zeta < 0.25$), the difference between radial and axial stress is insignificant and their governing equations remain valid.

With the proposed approach, if a fluid layer is assumed to exist between the penetrator and the surrounding medium, the resultant retarding force is obtained by replacing σ_{zz} with $-P_h$ in (3) where P_h (positive in compression) is the hydrostatic pressure in the fluid. One possibility is to choose $-P_h$ equal to the normal component of the traction, which varies as a function of time (nose penetration depth). Another variation is to choose $-P_h$ equal to the maximum value of the radial stress, which occurs when the nose is completely submerged. This assumption comes closest to simulating the results of Longcope and

Forrestal (1983), who obtained a value of radial stress at the penetrator surface that is independent of time as a consequence of their similarity procedure.

Any assumption involving a fluid layer leaves the possible contradictions concerning continuity of traction and motion of the fluid layer unresolved. Nevertheless, such assumptions are convenient, and, as this study shows, the differences in predicted retardation forces associated with various assumptions are not that great.

Equations of motion and deformation

A material description is used in which R, Z and θ are the Lagrangian coordinates. Since there is no rotation with the one-dimensional assumption, the rotation tensor, $\mathbf{R}$, is identical to the identity tensor, $\mathbf{I}$, and the deformation gradient with respect to the material frame, $\mathbf{F} = \text{Grad}\,\mathbf{r}$, for the current position, $\mathbf{r}$, equals the right stretch tensor:

$$\mathbf{F} = \mathbf{RU} = \mathbf{U}. \tag{8}$$

In terms of the radial displacement component, u, the physical components of $\mathbf{U}$ are:

$$[\mathbf{U}] = \begin{bmatrix} 1+u_{,R} & 0 & 0 \\ 0 & 1+\dfrac{u}{R} & 0 \\ 0 & 0 & 1 \end{bmatrix}. \tag{9}$$

The strain tensor, $\mathbf{E}$, is chosen to be $\ln(\mathbf{U})$ so that the physical components of $\mathbf{E}$ are:

$$E_{RR} = \ln(1+u_{,R}) \quad E_{ZZ} = 0 \quad E_{\theta\theta} = \ln\left(1+\frac{u}{R}\right). \tag{10}$$

Since the origin is a point in the domain of the problem, and the displacement at the origin is not zero, the circumferential strain is infinite at $R = 0$. It is assumed that the constitutive equation, which is given later, provides realistic values of stress under this condition.

The components of the Cauchy and rotated Cauchy stress tensors are identical. The only nonzero physical components are the diagonal terms σ_{RR}, σ_{ZZ} and $\sigma_{\theta\theta}$. With J defined as the determinant of $\mathbf{U}$, the equation of motion in the radial direction is

$$\frac{\partial}{\partial R}\left(\frac{J\sigma_{RR}}{1+u_{,R}}\right) + \frac{J}{R}\left(\frac{\sigma_{RR}}{1+u_{,R}} - \frac{\sigma_{\theta\theta}}{1+\dfrac{u}{R}}\right) = \rho_0 \ddot{u}; \tag{11}$$

in which the body force is assumed to be negligible, ρ_0 is the mass density in the undeformed configuration, and a superposed dot denotes a derivative with respect to time.

Weak formulations

For the finite element approach, weak formulations of both the equation of motion and the strain–displacement relations are used. For an element which is complete in first-order polynomials, element shape functions in the master element space are $N_1 = 1-\eta$ and $N_2 = \eta$ in which $\eta = (R - R_1^e)/h$ and R_1^e denotes the coordinate of the element node closest to the origin. All elements are assigned the same length, h. For weighting functions which are constant but arbitrary over each element, the weak form of (10) becomes a set of equations solved on an element-by-element basis:

$$\int_{D^e} [E^e_{RR} - \ln(1+u^e_{,R})]\, R\, \mathrm{d}R = 0$$

$$\int_{D^e} \left[E^e_{\theta\theta} - \ln\left(1+\frac{u}{R}\right)\right] R\, \mathrm{d}R = 0; \tag{12}$$

in which the superscript e identifies the element and D denotes the domain of the element. The volume element is proportional to $R\,\mathrm{d}R$. Each strain component is assumed to be constant over an element while the usual representation is used for the displacement: $u^e = u^e_1 N_1 + u^e_2 N_2$. With one-point quadrature, (12) yields:

$$E^e_{RR} = \ln\left(1+\frac{u^e_2 - u^e_1}{h}\right) \quad E^e_{\theta\theta} = \ln\left(1+\frac{u^e_1+u^e_2}{2R^e_1+h}\right). \tag{13}$$

The smoothing associated with the weak form removes the singularity in the circumferential strain for the element which contains the origin. It is assumed that the predicted values for stresses are accurate for a sufficiently refined mesh.

A weak form of the equation of motion is obtained by multiplying each term of (11) by a weight function, w, and integrating over the domain, $0 \leqslant R \leqslant R_M$, where the maximum value of R must be specified as part of each problem so that wave reflections do not contaminate the solution of interest near the penetrator. To maintain a symmetric formulation, the volume differential $R\,\mathrm{d}R$ is used instead of the area differential, $\mathrm{d}R$, which is used sometimes to transform axially symmetric formulations into forms similar to plane problems in Cartesian systems. After an integration by parts, the weak form is

$$\int_0^{R_M} \left[\rho_0 R w \ddot{u} + w_{,R} \frac{RJ\sigma_{RR}}{1+u_{,R}} + w \frac{J\sigma_{\theta\theta}}{1+\dfrac{u}{R}} \right] \mathrm{d}R - t_R R w|_0^{R_M} = 0 \quad \forall w; \tag{14}$$

in which

$$t_R = \frac{J\sigma_{RR}}{1+u_{,R}} n_R \tag{15}$$

is the radial component of the traction referred to the undeformed configuration and n_R is the radial component of the unit normal vector. If the displacement instead of the traction is prescribed, w must be zero at that point. The boundary term vanishes at the origin since $R = 0$, and a displacement condition is assumed at $R = R_M$ so the contribution from the boundaries is zero. With $w = w_1 N_1 + w_2 N_2$ and $R = R^e_1 + \eta h$ over each element, the result of performing the integration in (14) is that

$$[M]\{\ddot{u}\} + \{f^{\mathrm{I}}\} = \{0\}; \tag{16}$$

in which $\{u\}$ represents the vector of nodal displacements and

$$[M] = \sum_e [M^e] \quad \{f^{\mathrm{I}}\} = \sum_e \{f^{\mathrm{Ie}}\} \tag{17}$$

denote the mass matrix and internal force vector, respectively, obtained as the sum of contributions from each element. The element mass matrix is

$$[M^e] = \rho_0 h R_1^e \begin{bmatrix} \frac{1}{3} + \frac{h^*}{12} & \frac{1}{6} + \frac{h^*}{12} \\ \frac{1}{6} + \frac{h^*}{12} & \frac{1}{3} + \frac{h^*}{4} \end{bmatrix} \quad h^* = \frac{h}{R_1^e}. \tag{18}$$

Note that all components remain nonzero when the node of an element is at the origin ($R_1^e = 0$). For direct time integration, a diagonal mass matrix is required. If such a matrix is obtained by summing the rows of the consistent matrix of (18), the result is

$$[M^e]_D = \rho_0 h R_1^e \begin{bmatrix} \frac{1}{2} + \frac{h^*}{6} & 0 \\ 0 & \frac{1}{2} + \frac{h^*}{3} \end{bmatrix}. \tag{19}$$

For large values of R_1^e, both matrices assume forms proportional to those obtained in plane Cartesian systems.

The internal force vector is obtained by assuming the stress components are consant over each element. One-point quadrature yields

$$\{f^{le}\} = \begin{Bmatrix} -s_{RR}^e \left(R_1^e + \frac{h}{2}\right)\left[1 + \frac{u_1^e + u_2^e}{2R_1^e + h}\right] + \frac{h}{2} s_{\theta\theta}^e \left[1 + \frac{u_2^e - u_1^e}{h}\right] \\ s_{RR}^e \left(R_1^e + \frac{h}{2}\right)\left[1 + \frac{u_1^e + u_2^e}{2R_1^e + h}\right] + \frac{h}{2} s_{\theta\theta}^e \left[1 + \frac{u_2^e - u_1^e}{h}\right] \end{Bmatrix}. \tag{20}$$

Time integration

Suppose displacements and velocities are given. With the use of a constitutive equation, a sweep over the elements provides strains and stresses. Internal force components are then computed and allocated to nodes. If M_{iD} denotes the diagonal component of the mass matrix associated with node i, the approximation to the acceleration for each node is obtained from

$$\ddot{u}_i^n = \frac{-f_i^1}{M_{iD}}; \tag{21}$$

in which the superscript n implies the acceleration is associated with the discrete time $t^n = ns$, $n = 1, 2, \ldots$ for a time step of s. The explicit integration

$$\dot{u}_i^{n+1} = \dot{u}_i^n + s\ddot{u}_i^n \quad u_i^{n+1} = u_i^n + s\dot{u}_i^{n+1} \tag{22}$$

provides updated approximations for velocity and displacement. The process is repeated until the complete time history is obtained. The procedure is conditionally stable, so the time step must be less than the critical value which varies with the deformation since the problem is nonlinear. Here, one-tenth of the initial critical time step is used to obtain the complete solution and numerical stability is demonstrated by the existence of finite values for displacement.

Constitutive equation

Although the problem is one-dimensional, all three principal components of stress and strain are different. In order to make the problem analytically tractable, Longcope and Forrestal (1983) made the assumption that the circumferential and axial components of stress are equal. Here there is no need to make such an assumption and, as a side benefit of the numerical approach, the reasonableness of their assumption can be evaluated.

Conventional constitutive equations for geological materials are given by Desai and Siriwardane (1984). Because of the complexity of the problem and to preclude the need for a large number of material parameters, only elementary versions of such models are considered here.

For an isotropic, linearly elastic material, the relation between components of stress and elastic strain is:

$$\boldsymbol{\sigma} = \mathbf{C} : \mathbf{E}^{\mathrm{el}}; \tag{23}$$

in which $\mathbf{C}$ denotes the isotropic elasticity tensor given by

$$\mathbf{C} = \lambda \mathbf{i} \otimes \mathbf{i} + G\mathbf{I} \tag{24}$$

in terms of the Lamé constants λ and G. The second- and fourth-order identity tensors are $\mathbf{i}$ and $\mathbf{I}$, respectively. If the volumetric and deviatoric components of stress and strain are defined by the equations:

$$\boldsymbol{\sigma}^{\mathrm{d}} = \boldsymbol{\sigma} + P\mathbf{i} \quad P = -(\mathrm{tr}\,\boldsymbol{\sigma})/3 \quad \mathbf{E}^{\mathrm{eld}} = \mathbf{E}^{\mathrm{el}} + \tfrac{1}{3}E^{\mathrm{elv}}\mathbf{i} \quad E^{\mathrm{elv}} = -\mathrm{tr}\,\mathbf{E}^{\mathrm{el}}; \tag{25}$$

in which tr denotes the trace, an alternative form of (24) is

$$\boldsymbol{\sigma}^{\mathrm{d}} = 2G\mathbf{E}^{\mathrm{eld}} \quad P = \kappa E^{\mathrm{elv}}; \tag{26}$$

in which $\kappa = \lambda + \frac{2}{3}G$ is the bulk modulus. To allow for the possibility of a nonlinearly elastic bulk behavior, the bulk modulus is allowed to vary with elastic volumetric strain as follows:

$$\kappa = \kappa_0[1 + h(E^{\mathrm{elv}})^2]; \tag{27}$$

in which κ_0 and h are material constants to be determined from experimental data.

The inelastic behavior of geological materials is simulated with the use of the theory of plasticity. It is assumed that the total differential of strain consists of elastic and plastic parts:

$$\mathrm{d}\mathbf{E} = \mathrm{d}\mathbf{E}^{\mathrm{el}} + \mathrm{d}\mathbf{E}^{\mathrm{pl}}. \tag{28}$$

The plastic differential is obtained from the flow rule

$$\mathrm{d}\mathbf{E}^{\mathrm{pl}} = \mathrm{d}\lambda(\partial g/\partial \boldsymbol{\sigma}), \tag{29}$$

in which g is the plastic potential. The increment (positive) in the parameter λ is chosen such that the consistency condition $\mathrm{d}f = 0$ is satisfied, where the yield function, f, is given in terms of the invariants of stress and plastic strain. The yield condition $f = 0$ is defined such that $f < 0$ denotes an elastic state. Rate dependence is introduced through the overstress model of Malvern (1951) and Perzyna (1966) as follows:

$$\dot{\mathbf{E}}^{\mathrm{pl}} = \gamma(\langle f \rangle)(\partial g/\partial \boldsymbol{\sigma}); \quad \begin{array}{ll} \langle f \rangle = f & \text{if} \quad f > 0 \\ \langle f \rangle = 0 & \text{if} \quad f \leqslant 0. \end{array} \tag{30}$$

Strain hardening and softening models of the Prager–Drucker type are obtained by selecting f to be of the form

$$f \equiv f_{\mathrm{PD}} = \bar{s} - H; \tag{31}$$

in which

$$\bar{s} = [\tfrac{1}{2}\,\mathrm{tr}\,(\boldsymbol{\sigma}^{\mathrm{d}} : \boldsymbol{\sigma}^{\mathrm{d}})]^{1/2} \tag{32}$$

is an invariant of the stress deviator (tr denotes the trace). H depends linearly on P and nonlinearly on a plastic strain path invariant, defined in terms of the deviatoric part of the plastic strain as follows:

$$E^{\mathrm{p}} = \int [\tfrac{2}{3}\,\mathrm{tr}\,(\mathrm{d}\mathbf{E}^{\mathrm{pld}}\,\mathrm{d}\mathbf{E}^{\mathrm{pld}})]^{1/2}. \tag{33}$$

The specific functional form assumed for strain hardening is

$$H = H_0 + (H_{\mathrm{L}} - H_0)\sin\left[\frac{\pi}{2}\left(\frac{E^{\mathrm{p}}}{E^{\mathrm{p}}_{\mathrm{f}}}\right)^{n}\right] \quad 0 \leqslant E^{\mathrm{p}} \leqslant E^{\mathrm{p}}_{\mathrm{f}}$$

$$H_{\mathrm{L}} = \left(1 - \frac{\mu}{3}\right) f_{\mathrm{c}} + \mu P; \tag{34}$$

in which $E^{\mathrm{p}}_{\mathrm{f}}$ is the value of E^{p} at the limit state. There is an implicit assumption that the same value of $E^{\mathrm{p}}_{\mathrm{f}}$ is obtained at the limit state no matter which path is followed in stress space. The assumption is not valid in general but, for the current application where stress paths are similar, the asumption should not affect conclusions concerning other features of the constitutive model. The limiting value of the hardening function, H_{L}, is linear in P with the slope, μ, obtained from experimental data. The limit stress in uniaxial compression is f_{c}. The value of the hardening function at which inelasticity is first detected is denoted by H_0 for which a reasonable choice is $H_{\mathrm{L}}/2$. The shape of the strain hardening part of a stress–strain curve is governed by n, for which a typical value is 1/2.

If strain softening is assumed to occur, the function, H, decreases when E^{p} exceeds $E^{\mathrm{p}}_{\mathrm{f}}$. A functional form which is continuous and has a continuous first derivative with the hardening function at the limit state, $E^{\mathrm{p}} = E^{\mathrm{p}}_{\mathrm{f}}$, is given by:

$$H = H_a + (H_{\mathrm{L}} - H_a)(1 + aE^*)\,\mathrm{e}^{-aE^*} \quad E^{\mathrm{p}} > E^{\mathrm{p}}_{\mathrm{f}}$$

$$E^* = (E^{\mathrm{p}} - E^{\mathrm{p}}_{\mathrm{f}})/E^{\mathrm{p}}_{\mathrm{f}}. \tag{35}$$

The function decreases monotonically with E^* from H_{L} and asymptotically approaches the value H_a at a rate governed by the parameter a. Since strain softening is frequently accompanied by localization, it is not possible to correlate softening parameters with experimental data in a direct manner. Indirect correlation is possible in some cases but, here, the interest is an attempt to associate observed patterns with general features such as softening. No strain softening is predicted if $H_a = H_{\mathrm{L}}$. At least a small positive value for H_a is usually necessary to preclude numerical ringing.

For many soils, a yield surface in the deviatoric space in the form of an irregular hexagonal pyramid, described by the Mohr–Coulomb criterion, is considered to be more appropriate than the circular Prager–Drucker surface. The Mohr–Coulomb yield function is

$$f_{\mathrm{MC}} = \tau^* - s^* \sin\phi - \bar{c}\cos\phi, \tag{36}$$

where τ^* and s^* are the maximum shear and mean pressure, respectively, in a plane; $\bar{c}$ is the cohesion, and ϕ denotes the angle of internal friction. A hardening and softening formulation analogous to that given for the Prager–Drucker form is to let

$$H_{\mathrm{L}} = s^* \sin\phi - \bar{c}\cos\phi \tag{37}$$

and to write the yield function in the form $f_{\mathrm{MC}} = \tau^* - H$.

To preclude the excessive dilatation obtained from an associated flow rule, the plastic potential $g = \bar{s}$ is used with both the Prager–Drucker and Mohr–Coulomb yield functions. However, such a rule also implies that there is no inelastic volumetric compression, which is not realistic. To overcome this deficiency a simple planar cap is incorporated, as described by the yield function

$$f_{pc} = P - P_0 - c_1(e^{-c_2 E^{pl_v}} - 1) - c_3(1 - e^{-c_4 E^{pl_v}}); \tag{38}$$

in which P_0 is the pressure at which inelastic deformation first occurs. Other material parameters are c_1, c_2, c_3 and c_4. The two terms involving exponentials provide the characteristic features of stiffness softening and then hardening which are exhibited by the hydrostat for many soils. The cap is activated only by compressive stresses so that E^{pl_v}, the plastic volumetric strain, is a montonically increasing function obtained (with due regard for the sign) from an associated flow rule for the cap. For a volumetric strain rate effect, the corresponding overstress formulation is

$$\dot{E}^{pl_v} = \gamma_c \langle f_c \rangle \frac{\partial f_c}{\partial P} = \gamma_c \langle f_c \rangle; \tag{39}$$

in which γ_c is a viscosity parameter determined from experimental data.

VERIFICATION OF COMPUTATIONAL APPROACH

Linearly elastic problem

One way to ensure, as far as possible, that the numerical algorithm is accurate is to compare numerical and analytical solutions. One class of problems to which analytical solutions exist consists of a cylindrical cavity in an infinite domain with the boundary of the cavity loaded axisymmetrically by either a displacement or traction prescribed function. The problem is one of plane strain and is governed by the system of equations given in the previous section. Selberg (1951) gives an analytical solution for isotropic, elastic media where the radius of the cavity is R_0 and the boundary of the cavity is subjected to a unit step pressure when time is zero. If c is the radial wave velocity, then a dimensionless time is defined as $t' = [ct - (R - R_0)]/R_0$. For $R/R_0 = 2$, and for scaled stresses $\sigma'_{RR} = \sigma_{RR}\sqrt{R/R_0}$ and $\sigma'_{\theta\theta} = \sigma_{\theta\theta}\sqrt{R/R_0}$, plots of analytical and numerical solutions are given in Fig. 2. The two solutions agree, except for numerical dispersion.

Longcope and Forrestal (1983) provide an analytical solution for the distribution of radial stress for a conical nose ($\tan\alpha = 1/3$, $R_L = 0.078$ m) penetrating antelope tuff. They used an elastic–perfectly plastic Mohr–Coulomb model with elastic moduli consisting of the bulk modulus $\kappa = \kappa_0 = 2.0$ GPa (obtained by a linear fit to hydrostatic experimental data) and Poisson's ratio $\nu = 0.234$. For this problem, the Mohr–Coulomb criterion reduces

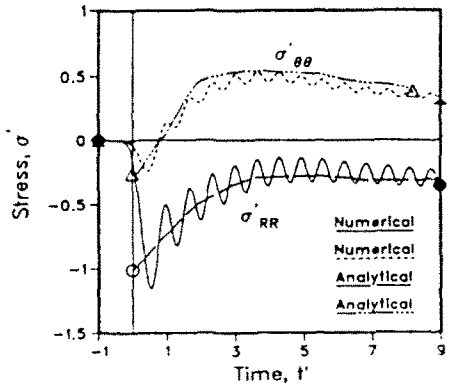

Fig. 2. Radial and circumferential stresses as functions of time at $R/R_0 = 2$.

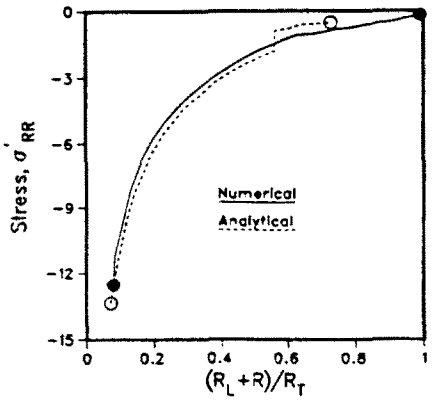

Fig. 3. Radial stress as a function of position at time $t = t_T$.

to $\sigma_{RR}-\sigma_{\theta\theta} = [1-(\mu/3)]f_c+\mu P$ with $f_c = 15$ MPa and $\mu = 1$. Neither a cap nor nonlinear elasticity is used to modify the linear pressure–volumetric strain relation. The initial mass density is $\rho_0 = 1620$ kg m^{-3} and the velocity of the penetrator is $v_p = 385$ m s^{-1}. Therefore, the total time of interest (the time of penetration), for a nose of length $L = 0.26$ m, is $t_T = L/v_p = 0.675\times10^{-3}$ s. The physical domain must be sufficiently large so that an elastic wave does not reflect off the far boundary and contaminate the solution. The domain used here is $R_T = ct_T$ with a pressure wave velocity of $c = \sqrt{\kappa/\rho_0}$. The analytical approach was mimicked in the sense that the flow rule was modified to meet the assumption that $\sigma_{zz} = \sigma_{\theta\theta}$. With a shift to the coordinate used for the analytical approach, the final distribution of the dimensionless stress $\sigma'_{RR} = \sigma_{RR}/f_c$ is given in Fig. 3 which shows good correlation between numerical and analytical results. The next section gives numerical results for cases where the assumptions inherent with the analytical solution are relaxed.

OTHER NUMERICAL SOLUTIONS

Elastic-perfectly plastic models

Instead of invoking the assumption that the axial and circumferential stresses are equal, the penetration problem from the previous section was analyzed for both a Mohr–Coulomb and a Prager–Drucker yield surface and with the nonassociated flow rule described previously. Other than for this modification, all other aspects of the model and values for material parameters were unchanged. The results obtained for the two yield functions were barely distinguishable and the same conclusion was obtained when more complicating features were added to the models. Since the Prager–Drucker model results in a more efficient numerical algorithm, only predictions obtained with this model are presented for the remainder of the paper.

For the penetrator problem, the evolution of the dimensionless stress components (actual stress divided by f_c) in the first element is given in Fig. 4 in which $t' = t/t_T$. Contrary to the assumption made to obtain the analytical solution, all stress components are significantly different, although $\sigma_{zz} = 1/2(\sigma_{\theta\theta}+\sigma_{RR})$ which is a consequence of the flow rule and a condition of plane strain. With the displacement at the origin prescribed, there is the implicit assumption that the coefficient of friction varies according to (7).

Strain hardening formulations

A strain hardening version of the Prager–Drucker yield function with no softening is given by (34) and (35) with $H_a = H_L$. Based on fits to triaxial compression data (Cooley, 1979), the hardening parameters are: $H_0 = H_L/2$, $E_L^T = 0.15$ and $n = 0.5$. With this modification, the magnitudes of all the stress components dropped from those of Fig. 4 by approximately 10%. Therefore, strain hardening was retained for all the subsequent analyses.

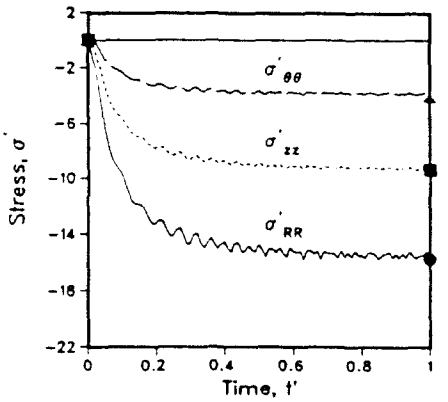

Fig. 4. Temporal plot of radial, circumferential and axial stress components in the first element.

The use of a hydrostat based on linear elasticity is clearly inappropriate if volumetric strains are predicted beyond those for which experimental data are available. To fit the data and to provide realistic extrapolated shapes for the hydrostat, both nonlinear elasticity and a plastic cap are invoked through (27) and (38). With $c_1 = 5 \times 10^6$, $c_2 = -40$, $c_3 = 50 \times 10^6$ and $c_4 = 50$, the fit to the experimentally obtained hydrostat under static conditions (Cooley, 1979) is shown in Fig. 5 for $\kappa_0 = 6.7$ GPa, $b = 0$ (linear elasticity) and $b = 100$ (nonlinear elasticity).The curve that includes the effect of nonlinear elasticity is more representative of typical hydrostats. As an example, Fig. 6 shows the effect of the parameter c_1 for $b = 0$, and similar plots show that the effects of the other parameters are easily obtained to assist in matching data for other materials.

Because the hydrostat is extrapolated as a monotonically increasing function past the set of experimental data shown in Fig. 5, the use of linear elasticity and the cap result in an increase in the magnitude of all the stress components of about 8%. Nonlinear elasticity results in a further increase, although the increase is not as great as might be expected because an increase in stiffness results in a decrease in the maximum strain. The addition of the cap counterbalances the use of strain hardening associated with the Prager–Drucker surface and so an example is already available as to why the use of simplified models may provide reasonable results. Nevertheless, for numerical solutions, there is no reason why features, which are known to be present, should not be included in constitutive models. Therefore, in subsequent analyses, strain hardening for both surfaces is retained but nonlinear elasticity is not included because the experimental data are not discriminating enough to justify such a degree of sophistication.

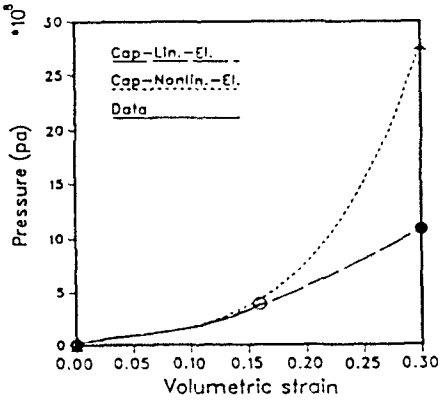

Fig. 5. Pressure–volume curve for experimental data and cap model with linear and nonlinear elasticity.

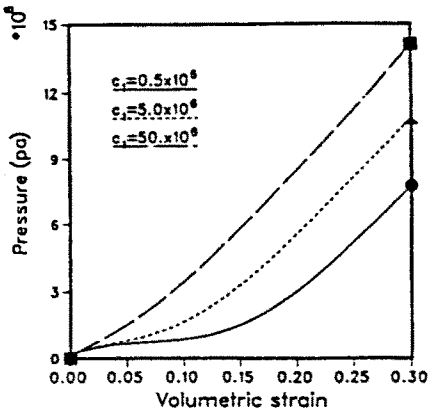

Fig. 6. Pressure–volume curve for $c_2 = -40$, $c_3 = 5 \times 10^6$, $c_4 = 50$ and various values of c_1.

Rate effects

It is extremely difficult to perform experiments involving large strain rates to determine, first, if a rate effect exists and, second, if a rate effect exists to evaluate pertinent material parameters. Here, a rate effect is postulated and predictions are made to see if such an effect is significant enough to be discernable from experimental data.

When a rate effect is added to the Prager–Drucker surface with a linearly-elastic hydrostat, there is essentially no change in predicted stresses from those obtained with no rate effect. This puzzling result was resolved by observing that the stress path for an element adjacent to the penetrator is essentially tangential to the limit surface so that no rate effect is activated. There is also considerable ringing of the stresses due to oscillations along the circular yield surface in the deviatoric plane. The overstress version of the Prager–Drucker surface is not pursued further.

As might be expected, an overstress cap model shows significant rate effects. The penetration problem under consideration exhibits strain rates up to about 5000 s^{-1}. The choice of $\gamma_c = 10^8\ s^{-1}$ yields the given static hydrostat for a strain rate of 1 s^{-1}, and a linear hydrostat with slope κ_0 at a constant strain rate of 5000 s^{-1}. The result of using such an overstress model is an increase in the magnitude of each stress component of approximately 20%. The overstress cap is retained in subsequent analyses.

Strain softening

Similar to the situation concerning rate effects, the strain softening assumption was made to determine if penetration data could be used to support or disprove such a hypothesis. The strain softening function is given in (35). The effect of the parameter, a, is shown in Fig. 7 for a uniaxial compressive stress path with $H_a = 0.2H_L$. For the penetrator

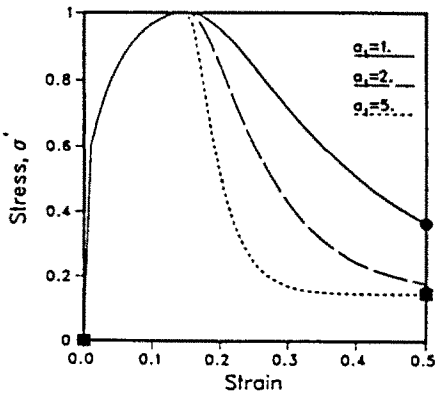

Fig. 7. Uniaxial compressive stress–strain curves showing the effect of the parameter a.

problem, the corresponding stresses in the first element as functions of time are shown in Fig. 8(a). After a time corresponding to about 40% of the total penetration time, the stresses were constant and nearly equal. Figure 8(b) shows the stress evolution when $H_1 = 0.01 H_0$. A hydrostatic state of stress is eventually displayed. Furthermore, the magnitude of the axial component of stress is much higher than for cases where softening is not invoked, with the result that the predicted retardation force on the penetrator increases with strain softening. An increase in the parameter, a, causes the hydrostatic state to appear more quickly. The evolution to the hydrostatic state is shown in Fig. 9(a), which displays the stress path in the space of P and $\bar{\tau}$.

Predictions of penetrator forces

Numerical analyses were also performed for a conical penetrator with $\tan \alpha = 1.4$, and for an ogival penetrator with $C_{RH} = 6$ for a range of velocities. Severe numerical oscillations started to appear for the ogive because, as shown in Fig. 9(b), the stress path reverses direction and approaches the origin, which is an indication that separation is imminent. Since the algorithm is restricted to a displacement prescribed boundary condition, separation is simulated by assigning zero to the stress components in the first element. Then the calculations can proceed without numerical instabilities.

Plots of maximum predicted retarding forces on penetrators are shown in Figs 10(a), 10(b) and 10(c), together with experimental data obtained by Forrestal and Grady (1982) and Forrestal *et al.* (1984a, 1986). The nomenclature used in the plots is as follows: PDHC denotes the hardening Prager Drucker and cap model, PDHCO indicates the previous model but with overstress viscoplasticity added, and PDHCOSF is the model with strain

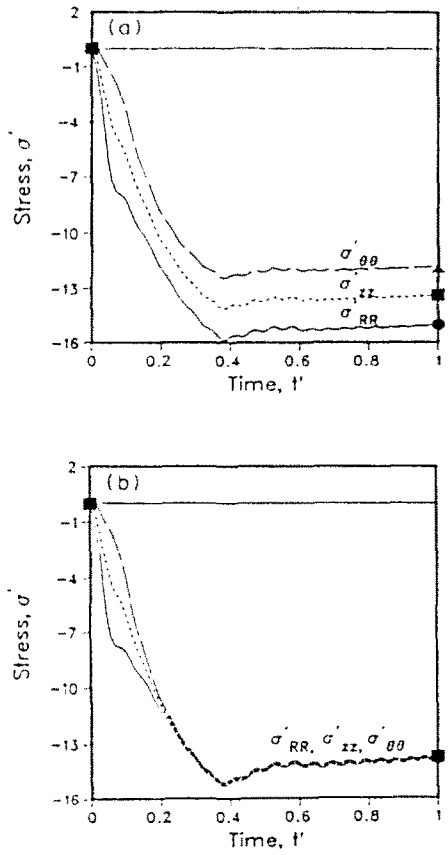

Fig. 8. The effect of strain softening on the evolution of stress components with time. (a) $a = 2$ and $H_1 = 0.2 H_0$, and (b) $a = 2$ and $H_1 = 0.01 H_0$.

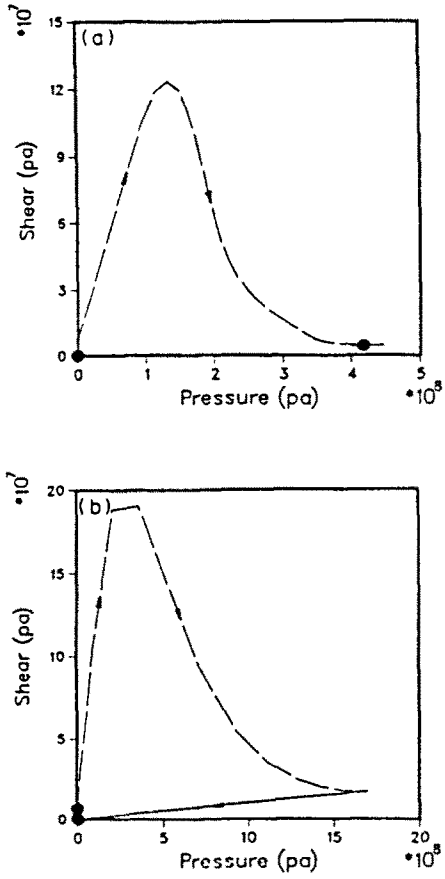

Fig. 9. Stress path in shear-pressure space. (a) Conical penetrator with tan $\alpha = 1/3$, and (b) ogival penetrator with $C_{RH} = 6$.

softening added to the other features. For each penetrator geometry, the rate independent model yields a penetrator force which is too low except for the lowest penetrator velocities. For the majority of the velocity range, the overstress model without strain softening provides reasonable agreement with experimental data while, generally speaking, the addition of strain softening yields forces significantly above those indicated by experiments. However, the one-dimensional assumption used for this analysis involves a kinematic constraint which would be relaxed in a two-dimensional analysis, in which case the agreement with experimental data using the strain softening aspect might be acceptable.

These analyses for penetration force are based on the displacement prescribed condition at the origin which is equivalent to invoking Coulomb's law with a variable coefficient of friction, as given by (7). To evaluate the possible effect of an assumption involving a hydrostatic layer, Figs 11(a) and 11(b) show predicted forces for a conical penetrator (tan $\alpha = 1/3$) in which the strain hardening rate-independent and rate-dependent models are used. For these figures the nomenclature is as follows: $p = \sigma_{RR}$ indicates that the pressure in the hydrostatic layer is set equal to the radial stress in the first element, $p = m$ denotes a pressure equal to the normal component of the traction, and $p = (\sigma_{RR})_{max}$ is the assumption that the pressure is equal to the maximum value of the radial stress. The first and last cases lead to a simple analytical equation. As Figs 11(a) and 11(b) show, each of these assumptions yields values of predicted forces above those provided by the displacement prescribed condition. In fact, the combination of a rate-independent model and two of the hydrostatic layer assumptions provides very good correlation with experimental data, which is another example of compensating effects. Another observation is that the assumption of a hydrostatic layer provides an increase in the predicted force in a manner completely consistent with that obtained through the use of strain softening.

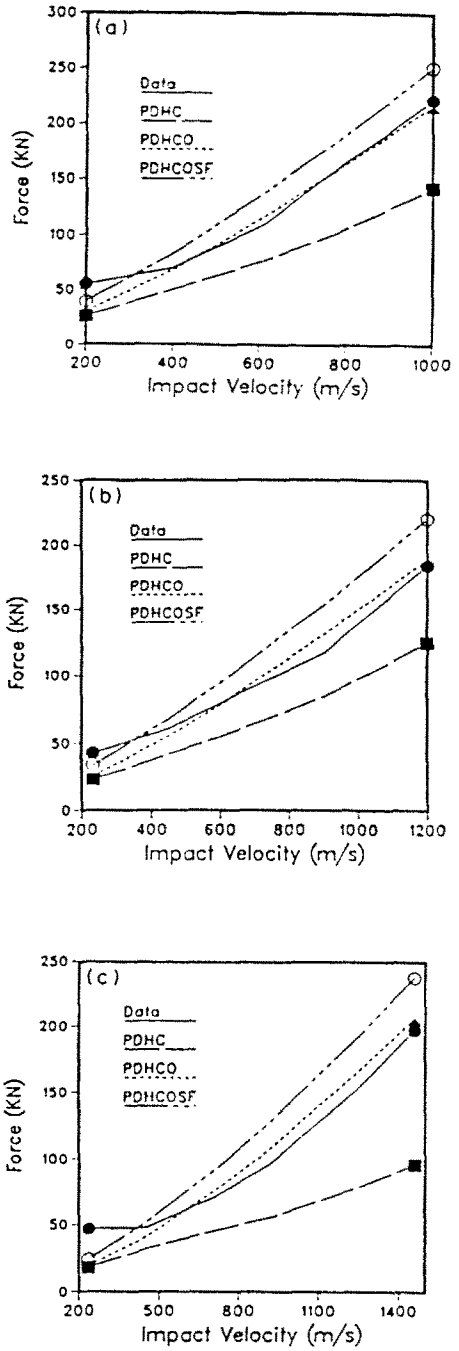

Fig. 10. Maximum axial force as a function of penetrator velocity. (a) Conical penetrator with $\tan \alpha = 1/3$, (b) conical penetrator with $\tan \alpha = 1.4$, and (c) ogival penetrator with $C_{RH} = 6$.

Convergence

With explicit time integration, the critical time step is of the order of the minimum time required for a wave to be transmitted across any element in the mesh. As deformation occurs, the critical time step may decrease; however, it is convenient to use a single time step for each problem. For each of the above calculations, a time step of 5% of the initial transit time of an element for a domain (variable) spanned by 50 uniform elements is used. Because the problem is nonlinear there is the ligitimate question as to whether or not the time step and element length are small enough. To indicate that the chosen increments are satisfactory, the conical penetrator with $\tan \alpha = 1/3$ and the model designated as PDHCO

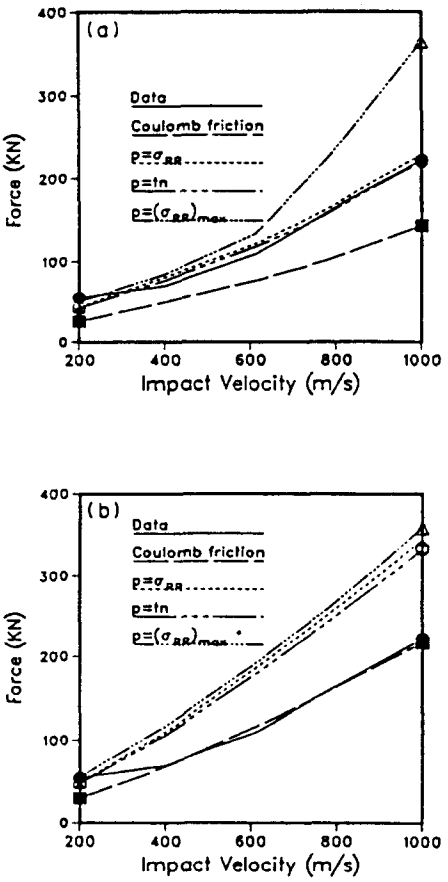

Fig. 11. Maximum axial force for a conical penetrator with tan $\alpha = 1/3$ and various interface assumptions. (a) Rate-independent model and (b) overstress rate-dependent model.

were used as a test case. When a time step of 1% of the initial transit time is used, the stress field is indistinguishable from the existing calculation. A comparison for time steps of 5% and 30% of the transit time is shown in Fig. 12 and again, there are insignificant differences. This result indicates that the selected time step is adequate. Figure 13(a) shows corresponding stress distributions for meshes involving 25 and 50 elements and significant differences are displayed. However, the difference in distributions obtained with 50 and 150 elements, as

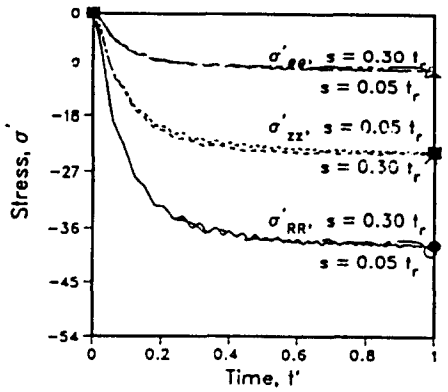

Fig. 12. Stresses in the first element for a conical penetrator with tan $\alpha = 1/3$, a penetration velocity of 614 m s^{-1} and for time steps of 5% and 30% of initial element transit time.

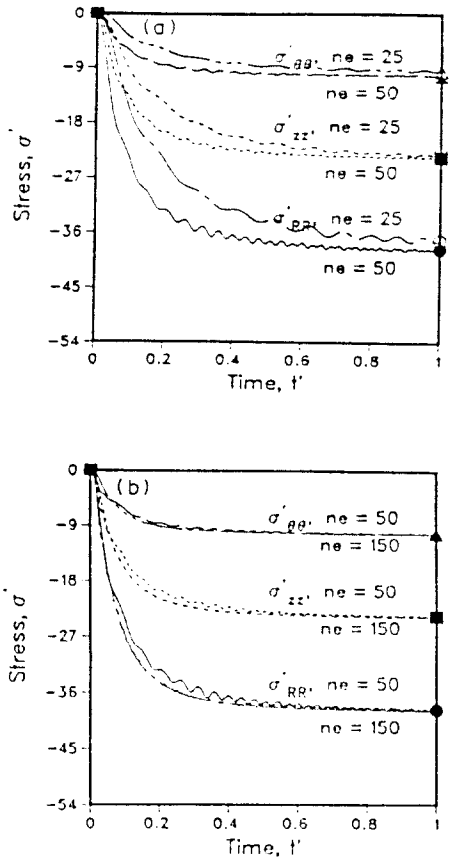

Fig. 13. Stress predictions for a conical penetrator with $\tan\alpha = 1.3$ and a penetration velocity of 614 m s^{-1}. (a) Results in the first and second elements for meshes of 25 and 50 elements, respectively, and (b) results in the first and third elements for meshes of 50 and 150 elements, respectively.

shown in Fig. 13(b), is not considered sufficiently large to warrant the increased computer time associated with the finer mesh.

CONCLUSIONS

This study shows that a numerical approach provides the means for evaluating a wide range of constitutive features, penetration velocities, penetrator shapes and interface assumptions for normal penetration in earth media. However, the one-dimensional assumption automatically implies Coulomb's law at the interface with a variable coefficient of friction. The assumption of a fluid layer, although included in the analysis, raises questions concerning the satisfaction of equations of motion in the layer.

Since the Mohr Coulomb and Prager Drucker models provided similar results, the latter was used for convenience. It was found that strain hardening of the Prager–Drucker surface is of some significance with regard to penetrator deceleration, but that the rate effect associated with this surface is not. The reason is that part of the stress trajectory for this class of problem is tangential to the limit surface and, therefore, the rate effect is not activated. However, for the cap part of the model, both strain hardening and rate effects are significant factors with regard to the retarding force on the penetrator.

The postulate of strain softening for the Prager Drucker surface causes the deformation to become more localized near the penetrator. An interesting result is that, with increased softening, the stress field adjacent to the penetrator becomes more hydrostatic in nature. This prediction is in accordance with the assumption based on experimental observations that a fluid-type layer appears to develop in many cases. However, here the

evolution of the layer is a consequence of the constitutive equation and is not the result of a separate assumption. An additional interesting point is that strain softening causes an increase in retardation force over the force obtained from the use of a nonsoftening model.

For many cases, the inclusion of realistic constitutive features results in a prediction of a retardation force above that indicated from experimental data. However, the one-dimensional assumption introduces a kinematical constraint that may be the cause for the higher prediction, in which case two-dimensional analyses might provide a better correlation with experimental data.

The analysis of the ogival nose indicates that above a critical velocity, separation occurs at some radius so that the segment of the penetrator beyond this radius does not contribute to the retardation force. This result raises the possibility of the existence of an optimal shape for producing the minimum retardation force. Again, a two-dimensional approach is probably warranted if there is a design requirement on shape optimization.

The original objective involved the possible use of penetrator data to evaluate the relative significance of constitutive features. These results show that there are countervailing mechanisms present which means considerable caution must be taken in drawing conclusions concerning the features of the penetrated medium based on penetrator acceleration data.

Acknowledgements—This research was supported by the Air Force Office of Scientific Research. Discussions with M. Forrestal and D. Longcope were particularly helpful.

REFERENCES

Backman, M. E. and Goldsmith, W. (1978). The mechanics of penetration of projectiles into targets. *Int. J. Engng Sci.* **16**, 1–99.

Byers, R. K. and Chabai, A. J. (1977). Penetration calculations and measurements for a layered soil target. *Int. J. Numer. Analyt. Meth. Geomech.* **1**, 107–138.

Byers, R. K., Chabai, A. J. and Walsh, R. T. (1975). Predictions of projectile penetration phenomena and comparison with experiments in a soil medium. SAND 75-0174, Sandia Laboratories, NM.

Byers, R. K., Yarrington, P. and Chabai, A. J. (1978). Dynamic penetration of soil media by slender projectiles. *Int. J. Engng Sci.* **16**, 835–844.

Chiu, C.-P. (1988). The theoretical effects of material models on the predicted response of the medium surrounding a penetrator. Ph.D. Dissertation, Department of Civil Engineering, The University of New Mexico.

Cooley, C. H. (1979). Testing program on TTR antelope tuff. Terra Tek, Salt Lake City, Utah, letter reports to Sandia National Laboratories, August 1979, July 1980 and January 1981.

Desai, C. S. and Siriwardene, H. J. (1984). *Constitutive Laws for Engineering Materials with Emphasis on Geologic Materials*. Prentice-Hall, Englewood Cliffs, NJ.

Forrestal, M. J. (1983). Forces on conical-nosed penetrators into targets with constant shear strength. *Mech. Mater.* **2**, 173–177.

Forrestal, M. J. (1985). Penetrators into dry porous rock. *Int. J. Solids Structures* **22**, 1485–1500.

Forrestal, M. J. and Grady, D. E. (1982). Penetration experiments for normal impact into geological targets. *Int. J. Solids Structures* **18**, 229–234.

Forrestal, M. J. and Longcope, D. B. (1982). Closed-form solutions for forces on conical-nosed penetrators into geological targets with constant shear strength. SAND 82-1177J, Sandia Laboratories, NM.

Forrestal, M. J., Lee, L. M. and Jenrette, B. D. (1986). Laboratory-scale penetration experiments into geological targets to impact velocities of 2.1 km/s. *J. Appl. Mech.* **53**, 317–320.

Forrestal, M. J., Lee, L. M., Jenrette, B. D. and Setchell, R. E. (1984a). Gas-gun experiments determine forces on penetrators into geological targets. *J. Appl. Mech.* **51**, 602–607.

Forrestal, M. J., Longcope, D. B., Jenrette, B. D. and Lee, L. M. (1984b). Pressure-bar experiments determine forces on penetrators into geological targets. *Int. J. Imp. Engng* **2**, 231–238.

Forrestal, M. J., Longcope, D. B. and Norwood, F. R. (1981a). A model to estimate forces on conical penetrators into dry porous rock. *J. Appl. Mech.* **48**, 25–29.

Forrestal, M. J., Norwood, F. R. and Longcope, D. B. (1981b). Penetration into targets described by locked hydrostats and shear strength. *Int. J. Solids Structures* **17**, 915–924.

Longcope, D. B. and Forrestal, M. J. (1981). Closed-form approximations for forces on conical penetrators into dry porous rock. *J. Appl. Mech.* **48**, 971–972.

Longcope, D. B. and Forrestal, M. J. (1983). Penetration of targets described by a Mohr Coulomb failure criterion with a tension cutoff. *J. Appl. Mech.* **50**, 327–333.

Longcope, D. B. and Grady, D. E. (1978). Initial response of a rock penetrator. *J. Appl. Mech.* **45**, 559–564.

Malvern, L. E. (1951). The propagation of longitudinal waves of plastic deformation in a bar of material exhibiting a strain rate effect. *Trans. ASME J. Appl. Mech.* **18**, 203–208.

Norwood, F. R. (1974). Cylindrical cavity expansion in a locking soil. SLA-74-0201, Sandia Laboratories, NM.

Norwood, F. R. and Sears, M. P. (1982). A nonlinear model for the dynamics of penetration into geological targets. *J. Appl. Mech.* **49**, 26–30.

Perzyna, P. (1966). Fundamental problems in viscoplasticity. *Adv. Appl. Mech.* **9**, 243–377.

Selberg, H. L. (1951). Transient compression waves from spherical and cylindrical cavities. *Arkiv Fysik* **5**, 97–108.

Thigpen, L. (1974). Projectile penetration of elastic-plastic earth media. *J. Geotech. Engng Div., ASCE*, **100**, 279–293.

Young, C. W. (1969). Depth prediction for earth penetrating projectiles. *J. Soil Mech. Found., ASCE*, **SM3**, 803–817.

Young, C. W. (1972). Empirical equations for predicting penetration performance in layered earth materials for complex penetrator configurations. SC-DR-720523, Sandia Laboratories, NM.

Young, C. W. (1976) Status report on high velocity soil penetration program. SAND 76-0585, Sandia Laboratories, NM.